



SEMESTER THESIS

**Extended Model-Based Inference of Flame Transfer Matrices
from Acoustic Measurements**

Autor:

Thomas Hollweck

Matrikel-No:

03717838

Betreuer:

Alexander Eder, M. Sc.

Moritz Merk, M. Sc.

Prof. Wolfgang Polifke, Ph. D.

April 15, 2024

Erklärung

Hiermit versichere ich, die vorliegende Arbeit selbstständig verfasst zu haben. Ich habe keine anderen Quellen und Hilfsmittel als die angegebenen verwendet.

Garching, 15.04.2024

Ort, Datum

Thomas Hollweck

Acknowledgement

The concepts presented in Sec. 2, and in particular the visualization of the extended method in Fig. 2.2, were derived in collaboration between the author and the supervisors, Alexander J. Eder, M.Sc. and Moritz Merk, M.Sc..

Abstract

Accurate post-processing of the flame dynamics in complex test-rigs is crucial for maintaining reliable propulsion systems. In the presence of features, such as effusion hole cooling or flow within a bypass annulus, the established feedback loops prevent the application of conventional post-processing methods. Recent work proposed a general framework of model-based inference (MBI) methods applicable to complex combustor chambers. These methods employ a low-order-model (LOM) of a complex test rig to infer the flame transfer matrix (FTM) from a unique reactive transfer matrix measurement. This work extends the inference of a FTM by incorporating a single non-reactive transfer matrix measurement. The extended inference benefits from the additional measurement, as a substantial amount of systematic errors in the internal dynamics of the utilized LOM can be compensated. As a result, the identification gains robustness and identifies the FTM with higher accuracy for various systematic modeling errors.

Rewards of the proposed extended model-based inference method are demonstrated with regard to the Rolls-Royce Scaled Acoustic Rig for Low Emission Technology (SCARLET) operated under realistic engine conditions ($T_{in} \approx 825$ K, $p_{in} \approx 25$ bar, kerosene). Studies with randomized modeling errors are conducted with a LOM representing the SCARLET test-rig based on a generic FTM. Thereby, the impact of systematic correction on the inference method is analyzed. Ultimately, the novel approach is applied to measurement data to extract the FTM.

Contents

Nomenclature	vii
1 Introduction	1
2 Modeling Approach	3
2.1 Acoustic measurement of the combustor transfer matrix	3
2.2 Model-based inference of the FTM	3
2.3 Extension of the model-based inference with systematic corrections	6
2.4 Requirements on the LOM for a reduction of systematic errors	7
3 Modeling of the thermoacoustic test rig	9
3.1 Setup of the SCARLET test-rig	9
3.2 Low-order network modeling of the SCARLET test rig	10
3.3 Identification of substantial systematic modeling errors	12
4 Generic investigation with self-consistent LOM framework	15
4.1 General procedure of the statistical study	15
4.2 Comparison of MBI-methods by inspection of the identified FTM-elements	17
4.3 Sensitivity analysis of model-based inference methods	19
4.4 Correlation of systematical errors for hot and cold operating conditions	20
5 FTM inference with experimental data	22
5.1 Identification of FTM applying different procedures	22
5.2 Discussion	25
6 Conclusion and Outlook	27
Bibliography	28

Nomenclature

Abbreviation

FTF	Flame Transfer Function
FTM	Flame Transfer Matrix
MBI	model-based inference
MMM	multi-microphone-method

Greek Symbols

ϵ	relative error (H_∞ -norm)	[-]
------------	------------------------------------	-----

Superscripts

\sim	measurement
c	cold
h	hot
hc	hot and cold

Roman letters

B	Burner transfer matrix	[-]
C	Combustor transfer matrix	[-]
F	Flame transfer matrix	[-]
\mathcal{F}	Flame transfer function	[-]
T	Transfer matrix	[-]
A_{eff}	effective injector area	[m ²]
c	Speed of sound	[m s ⁻¹]

NOMENCLATURE

f, g	Acoustic Riemann invariants	[-]
n	number of acoustic paths (perforated liner)	[-]
p	Pressure	[kgm ⁻¹ s ⁻²]
u	Velocity	[m s ⁻¹]
X	flow split	[-]
x_{ref}	reference position	[m]
Z	Generalized parameter vector	[-]
M	Mach number	[-]

Subscripts

d	downstream
p	product
r	reactant
u	upstream

1 Introduction

A thorough understanding and a reliable prediction of thermoacoustic instabilities is crucial for the safe and efficient operation of combustion systems[23]. If the heat release within the flame is in phase with local pressure fluctuations, unstable modes may grow according to the Rayleigh criterion [31]. This significantly lowers the overall efficiency as the acoustic modes dissipate energy that cannot be used for propulsion. Furthermore, the acoustic modes may continuously increase in amplitude if the excitation exceeds the dissipation of acoustic energy [22], possibly leading to the destruction of the operating system.

Due to the variety of characteristic length scales in a thermoacoustic problem, low-order network models are often exploited [8, 9, 16, 24, 29]. They are comprised of single linearized compact and non-compact one-dimensional network elements to model a complex three-dimensional configuration [12]. The elements can be described as multiports with scattering matrices relating the Riemann Invariants f and g of an acoustic wave at the respective input and output ports. The utilized scattering matrices are either derived from partial differential equations or rely on measurements [12]. In the scope of a network model, the flame transfer matrix is a compact network element relating the acoustic fluctuations in the close vicinity upstream and downstream the flame. Based on a closure equation, e.g. the Rankine-Hugonot relations for fuel and air as ideal gases, the FTF can be extracted from the FTM[16].

Acoustic fluctuations within the system lead to fluctuations of the upstream velocity in the presence of acoustic feedback loops. In the scope of stability analysis, the flame transfer function relates the unsteady heat release rate with the acoustic fluctuations. Therefore, reliable measurements of the FTF are of particular interest to the development of new combustion chambers. Indirect measurements based on the multi-microphone method [5, 17, 25, 26, 27, 30] are favorable in terms of effort and applicability under real operating conditions [1]. In this method, the combustion chamber is positioned between two ducts equipped with several microphones. Pressure fluctuations upstream and downstream the combustion chamber are then measured under reactive and non-reactive conditions. The achieved pressure signals can be related to the Riemann invariants f and g using the overdetermined system of equations [6]. Accordingly, the hot and cold combustor transfer matrices, \tilde{C}^h and \tilde{C}^c can be obtained and serve as a basis for further post-processing of the FTM and consecutively, the FTF[2].

Under restrictive conditions, the FTM can be precisely obtained by matrix multiplication of \tilde{C}^h and \tilde{C}^c and a consecutive shift to the position of the compact flame within the test rig [4], referred to as BFTM-approach in this work. Likewise, further post-processing of the FTF from the FTM is realized with high fidelity [2]. This established procedure is equivalent to identifying the compact FTM in a network model, where the FTM is embedded into two ducts

with uniform and identical cross-section in the absence of any acoustic feedback loop [11]. Eder et al. have shown, that this post-processing method does not apply to more complex test rigs like the SCARLET-test rig [10]. In particular, varying cross-sections, additional acoustic coupling, and substantial mass flux through the perforated liners make the BFTM-approach inapplicable [11]. Recently, more sophisticated network models have been developed to post-process the FTM within complex test rigs following different approaches. If the acoustic feedback loop through the effusion holes is not encountered [1], the BFTM-approach could be extended to extract the FTM using a reactive and non-reactive measurement with similar inlet conditions. Contrary, Eder *et al.* [11] suggested extracting the FTM from a single hot measurement, thereby employing a network model with acoustic feedback loops for an inference of the FTM. Following this procedure, the non-reactive measurement is not part of the identification procedure. It solely serves as a reference for estimating the accuracy of the prediction or for optimization based on barely accessible parameters of the modeled test rig.

This raises the question, of whether the previous method proposed by Eder et al. can be further improved by incorporating a cold measurement in the prediction. As both hot and cold low-order models share systematic errors, the cold model could be utilized to derive a compensation for the systematic modeling error. The same compensation could then be applied to the hot model, which might reduce the systematic error in the model-based inference approach. Potentially, the MBI-method gains some positive features of the BFTM-approach, such as its high robustness. In the following, we refer to the model-based inference presented by Eder *et al.* [11] as the method MBI^h . The extension with a systematic correction derived in this work is referred to as MBI^{hc} .

This work presents a novel approach (MBI^{hc}) for the inference of a FTM from measurements of hot and cold combustor transfer matrices. The new method consistently extends the model-based inference as it employs a unique LOM for the inference of a single FTM from multiple measurements. The new technique is applied to the Rolls-Royce Scaled Acoustic Rig for Low Emission Technology (SCARLET) [13, 14], employing a sophisticated LOM [10, 11] for inference. The major focus is set on improvements of the extension MBI^{hc} compared to the classical model-based inference approach MBI^h .

This work is structured as follows. At first, we recap the derivation of the model-based inference (MBI) of an FTM and highlight the extensions towards the new method, MBI^{hc} (Sec. 2). Next, we evaluate the statistical improvements gained by applying a systematic correction using synthetic models with predefined systematic modeling errors. Finally, we apply the methods MBI^h and MBI^{hc} to real measurements of the combustor transfer matrices of the SCARLET test rig (Sec. 5), finishing with a conclusion in Sec. 6.

2 Modeling Approach

In the following, we will briefly recap the derivation of the model-based inference method as proposed by Eder et al. [11] and extend the method by including non-reactive measurements to systematically derive the extended MBI^{hc}-method. In this work, reactive and non-reactive conditions are referred to as hot and cold conditions, respectively.

2.1 Acoustic measurement of the combustor transfer matrix

In accordance with previous work of Eder et al. [11], measured transfer matrices are referred to as $\tilde{\mathbf{T}}$ and are generally acquired by means of the multi-microphone-method (MMM) [7, 21]. Measurements are taken at various positions upstream and downstream of the combustion chamber, indicated as pressure and velocity fluctuations p' and u' in Fig. 2.1. The measured combustor transfer matrix $\tilde{\mathbf{C}}^m$, $m \in \{h, c\}$ is therefore given by $\tilde{\mathbf{C}}^h$ for reactive (hot) conditions and by $\tilde{\mathbf{C}}^c$ for non-reactive, i.e. cold conditions.

$$\begin{pmatrix} \frac{p'}{\rho \tilde{c}} \\ u' \end{pmatrix}_{\tilde{d}} = \tilde{\mathbf{C}}^m \begin{pmatrix} \frac{p'}{\rho \tilde{c}} \\ u' \end{pmatrix}_{\tilde{u}}. \quad (2.1)$$

It relates the pressure and velocity fluctuations at two reference points $x_{\text{ref},u}$ and $x_{\text{ref},d}$ upstream of the burner and downstream of the combustor (Fig. 2.1). The reference positions coincide with the indices 'u' and 'd' in Fig. 2.1. The variables ρ and c represent the density and speed of sound at the respective reference positions which are referred to as \tilde{u} and \tilde{d} in the following derivations.

2.2 Model-based inference of the FTM

Fig. 2.1 displays the SCARLET test rig that encounters more complex features than simplistic test rigs, particularly embedding relevant acoustic feedback loops. The following network model describes the acoustics of such a test rig in a general manner [11], regardless of any extensions based on the mean flow or additional acoustic paths. The ports \tilde{u} and \tilde{d} are associated with the reference positions upstream and downstream utilized for the measurements of the global combustor transfer matrices $\tilde{\mathbf{C}}^h$ and $\tilde{\mathbf{C}}^c$. The ports 'r' and 'p' reflect the states at the positions upstream and downstream of the flame, which can be considered as a compact element. In this work, the states are chosen as the pressure and velocity fluctuations, i.e.

$$\mathbf{v}_i = \begin{pmatrix} \frac{p'}{\rho \tilde{c}} \\ u' \end{pmatrix}_i, \quad i \in \{u, d, r, p\}. \quad (2.2)$$

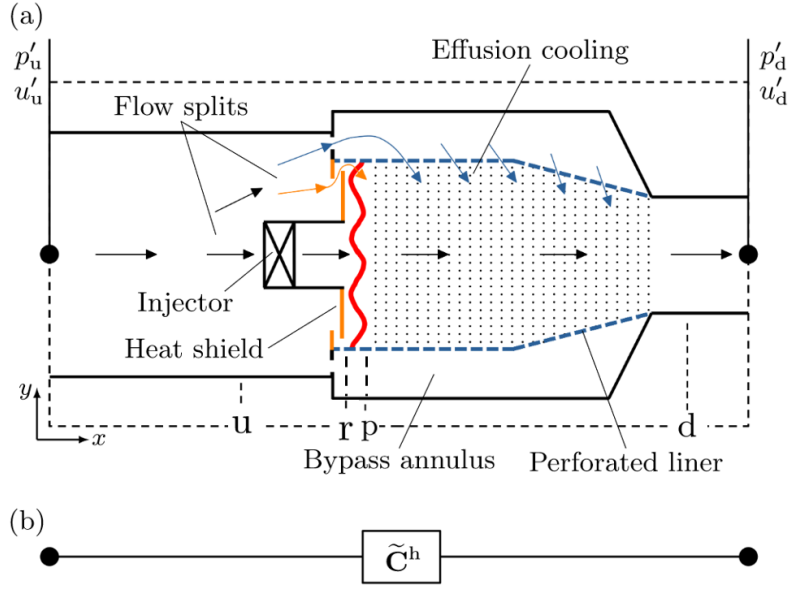


Figure 2.1: a) Schematic representation of the combustion chamber of a complex aero-engine test rig under reactive conditions. The reference positions of p' and u' correspond to the global dynamics $\tilde{\mathbf{C}}^h$ depicted in b). The indices 'u', 'r', 'p', and 'd' are abbreviations of upstream, reactants, products, and downstream, respectively. Figure from Eder *et al.*[11]

These fluctuations are related by a transfer matrix \mathbf{T} comprising a MIMO-system as

$$\begin{pmatrix} \mathbf{v}_r \\ \mathbf{v}_d \end{pmatrix} = \begin{pmatrix} \mathbf{T}_{ru} & \mathbf{T}_{rp} \\ \mathbf{T}_{du} & \mathbf{T}_{dp} \end{pmatrix} \begin{pmatrix} \mathbf{v}_u \\ \mathbf{v}_p \end{pmatrix}. \quad (2.3)$$

The model-based inference method of previous work[11] solely utilizes a hot measurement to identify the FTM, which is a major advantage in terms of practical applicability. The underlying procedure is illustrated in the upper part of Fig. 2.2 disregarding any light gray block as these blocks indicate the extension towards MBI^{hc} . Based on the hot connector model described by Eq. 2.3, the global dynamics, $\mathbf{v}_d = \tilde{\mathbf{C}}^h \mathbf{v}_u$, can be achieved for a choice of

$$\mathbf{F}^h := \left[\mathbf{T}_{ru}^h \left(\tilde{\mathbf{C}}^h - \mathbf{T}_{du}^h \right)^{-1} \mathbf{T}_{dp}^h + \mathbf{T}_{rp}^h \right]^{-1} \quad (2.4)$$

The FTM identified with the MBI^h -approach is referred to as a \mathbf{F}^h , indicating that the inference is based on single hot LOM and corresponding hot measurement. Eq. 2.4 emphasizes, that the internal dynamics \mathbf{T}^h of the hot connector model and the hot measurement $\tilde{\mathbf{C}}^h$ uniquely determine the FTM. The internal dynamics of the cold LOM, denoted as \mathbf{T}^c , can be described by Eq. 2.3, as well. The internal dynamics of \mathbf{T}^c and \mathbf{T}^h differ under hot and cold operating conditions. For instance, $\mathbf{T}_{ru}^h \neq \mathbf{T}_{ru}^c$. The same holds for the remaining submatrices in Eq. 2.3. As derived in previous work [11], the global combustor transfer matrix \mathbf{C}^c of the cold LOM is derived from Eq. 2.3 employing the relation $\mathbf{v}_r^c = \mathbf{I} \mathbf{v}_p^c$, as

$$\mathbf{C}^c = \mathbf{T}_{dp}^c \left(\mathbf{I} - \mathbf{T}_{rp}^c \right)^{-1} \mathbf{T}_{ru}^c + \mathbf{T}_{du}^c. \quad (2.5)$$

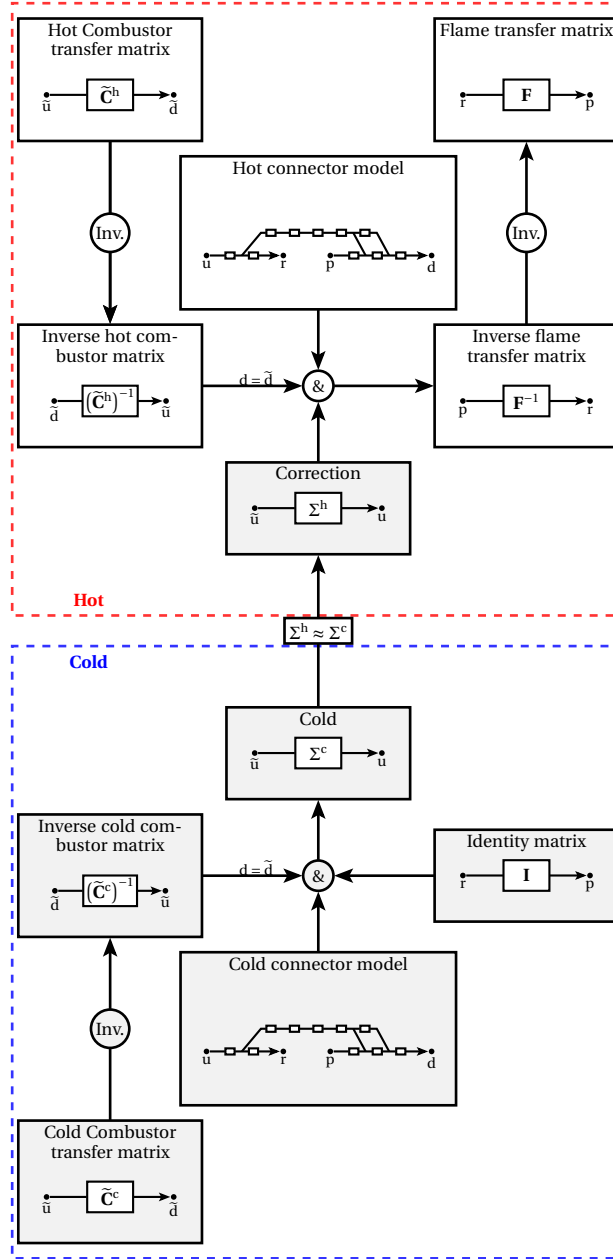


Figure 2.2: Visualization of the extended model-based inference procedure of the flame transfer matrix (MBI^{hc}) [18]; the classical model-based inference (MBI^{h}) is indicated in gray and does not include any correction based on a cold measurement. (a) a systematic compensation Σ^{c} is deduced from a cold acoustic measurement and a corresponding low-order network model and applied to the reactive network model as Σ^{h} . (b) A modified conservative closed-loop system of the hot model is achieved to gain the final open-loop system to extract \mathbf{F} .

The deviation of \mathbf{C}^c from a corresponding measurement $\tilde{\mathbf{C}}^c$ is the unique indicator for the accuracy of the inferred FTM, \mathbf{F}^h . Note, that the internal dynamics \mathbf{T}^c do not appear in the identification of Eq. 2.4.

2.3 Extension of the model-based inference with systematic corrections

Next, we derive the main steps for extending the MBI-method MBI^h given by Eq. 2.4. The systematic compensation is visualized in Fig. 2.2, now including the elements depicted in light gray. For non-reactive conditions, an accurate model approaches the global dynamics $\mathbf{v}_d^c = \tilde{\mathbf{C}}^c \mathbf{v}_u^c$ (Fig. 2.2, bottom left corner), from which the inverse global dynamics, $\mathbf{v}_u^c = (\tilde{\mathbf{C}}^c)^{-1} \mathbf{v}_d^c$, can be deduced. By definition, the state \mathbf{v}_d^c is considered equivalent to the state \mathbf{v}_d^c of the cold connector model. A cold connector model is only fully consistent if it equally matches the correct dynamics between the ports 'p' and 'r', i.e. $\mathbf{v}_p^c = \mathbf{I} \mathbf{v}_r^c$ (bottom, right). If and only if the cold LOM \mathbf{T}^c consistently models the global dynamics, equality holds for the states $\tilde{\mathbf{u}}$ and \mathbf{u} , i.e. $\mathbf{u} = \Sigma^c \tilde{\mathbf{u}} = \mathbf{I} \tilde{\mathbf{u}}$. On the contrary, inconsistencies are reflected in the transfer matrix Σ^c , thus being considered as the systematic compensation for the cold LOM (top, blue box). The systematic correction Σ^c is unique for a given internal dynamics \mathbf{T}^c and a measurement $\tilde{\mathbf{C}}^c$. The internal dynamics in terms of an arbitrary Σ^c [19] are given by

$$\begin{pmatrix} \mathbf{v}_r \\ \tilde{\mathbf{v}}_d \end{pmatrix} = \begin{pmatrix} \mathbf{T}_{ru}^c \Sigma^c & \mathbf{T}_{rp}^c \\ \mathbf{T}_{du}^c \Sigma^c & \mathbf{T}_{dp}^c \end{pmatrix} \begin{pmatrix} \tilde{\mathbf{v}}_u \\ \mathbf{v}_p \end{pmatrix} = \begin{pmatrix} \mathbf{0} & \mathbf{I} \\ \tilde{\mathbf{C}}^c & \mathbf{0} \end{pmatrix} \begin{pmatrix} \tilde{\mathbf{v}}_u \\ \mathbf{v}_p \end{pmatrix}. \quad (2.6)$$

A decoupling of the dynamics according to Eq. 2.6 can only be established if \mathbf{v}_p and $\tilde{\mathbf{v}}_u$ are dependent on each other, satisfying

$$\mathbf{v}_p = (\mathbf{I} - \mathbf{T}_{rp})^{-1} \mathbf{T}_{ru} \Sigma^c \tilde{\mathbf{v}}_u. \quad (2.7)$$

Consequently, the four unknown coefficients of Σ^c can be determined by solving the matrix equation

$$\begin{aligned} \left(\mathbf{T}_{du} \Sigma^c + \mathbf{T}_{dp} (\mathbf{I} - \mathbf{T}_{rp})^{-1} \mathbf{T}_{ru} \Sigma^c \right) \tilde{\mathbf{v}}_u &= \mathbf{0} \iff \\ \Sigma^c &= \left(\mathbf{T}_{du} + \mathbf{T}_{dp} (\mathbf{I} - \mathbf{T}_{rp})^{-1} \mathbf{T}_{ru} \right)^{-1}. \end{aligned} \quad (2.8)$$

Alanyaliouglu *et al.* [1] utilized the measurement $\tilde{\mathbf{C}}^c$ to optimize the cold and hot LOM through shared physical parameters [1]. The underlying assumption is that a similar systematic modeling error can be established and minimized for reactive and non-reactive operating conditions. A similar but more comprehensive approach is followed in this work, generalized towards systematic errors in the internal dynamics \mathbf{T} . Further following the scheme in Fig. 2.2, Σ^c is set equal to Σ^h . This accounts for the core assumption of a common systematic modeling error, considered as an intrinsic property of the utilized low-order model regardless of

the specific operating conditions. The correction Σ^c establishes a consistent LOM that models the correct global dynamics of $\tilde{\mathbf{C}}^c$ and \mathbf{I} . Likewise, applying an identical correction to the hot LOM establishes the consistent global dynamics in terms of $\tilde{\mathbf{C}}^h$ and the correct \mathbf{F} for correlated systematic errors. The model-based inference of \mathbf{F} based on MBI^{hc} is therefore given by

$$\begin{aligned} \mathbf{F}^{\text{hc}} &:= \left[\mathbf{T}_{\text{ru}}^{\text{h}} \Sigma^{\text{h}} \left(\tilde{\mathbf{C}}^{\text{h}} - \mathbf{T}_{\text{du}}^{\text{h}} \Sigma^{\text{h}} \right)^{-1} \mathbf{T}_{\text{dp}}^{\text{h}} + \mathbf{T}_{\text{rp}}^{\text{h}} \right]^{-1} \approx \\ &\approx \left[\mathbf{T}_{\text{ru}}^{\text{h}} \Sigma^{\text{c}} \left(\tilde{\mathbf{C}}^{\text{h}} - \mathbf{T}_{\text{du}}^{\text{h}} \Sigma^{\text{c}} \right)^{-1} \mathbf{T}_{\text{dp}}^{\text{h}} + \mathbf{T}_{\text{rp}}^{\text{h}} \right]^{-1} \end{aligned} \quad (2.9)$$

The superscripts 'hc' indicate model-based inference with both hot and cold LOMs and respective measurements.

2.4 Requirements on the LOM for a reduction of systematic errors

Errors of MIMO transfer functions are commonly described using the H_∞ -norm [3]. Therefore, the absolute and relative deviation of a complex-valued transfer matrix $\mathbf{T}_{n \times m}$ concerning a reference transfer matrix $\tilde{\mathbf{T}}_{n \times m}$ are computed as

$$\epsilon(\mathbf{T}) := \frac{\|\mathbf{T} - \tilde{\mathbf{T}}\|_\infty}{\|\tilde{\mathbf{T}}\|_\infty}. \quad (2.10)$$

Given for instance $\mathbf{T} = \mathbf{F}^{\text{hc}}$ (Eq. 2.9), and $\tilde{\mathbf{T}} = \tilde{\mathbf{F}}$, the accuracy of the inference methods MBI^{hc} can be estimated based on the error $\epsilon(\mathbf{F}^{\text{hc}})$. Note, that this theoretically requires a reference solution $\tilde{\mathbf{F}}$, which is often missing in real test-rigs such as the SCARLET test-rig [13, 14] assessed in this work.

Before the new method MBI^{hc} is applied to an exemplary LOM, the chances and limitations of this method are investigated in terms of reducible errors. At first, a reference connector model is introduced, describing the correct internal dynamics of a cold connector model as

$$\begin{pmatrix} \tilde{\mathbf{v}}_{\text{r}} \\ \tilde{\mathbf{v}}_{\text{d}} \end{pmatrix} = \begin{pmatrix} \tilde{\mathbf{T}}_{\text{ru}} & \tilde{\mathbf{T}}_{\text{rp}} \\ \tilde{\mathbf{T}}_{\text{du}} & \tilde{\mathbf{T}}_{\text{dp}} \end{pmatrix} \begin{pmatrix} \tilde{\mathbf{v}}_{\text{u}} \\ \tilde{\mathbf{v}}_{\text{p}} \end{pmatrix}. \quad (2.11)$$

Without loss of generality, independent disturbances ϵ_i can be applied to each input port as $\mathbf{v}_i = \epsilon_i \tilde{\mathbf{v}}_i$ for $i \in \{\text{u}, \text{p}\}$ and output port as $\tilde{\mathbf{v}}_i = \epsilon_i \mathbf{v}_i$ for $i \in \{\text{d}, \text{r}\}$, from which the dynamics of the utilized cold LOM in Eq. 2.3 [19], \mathbf{T}^c , can be generally derived as

$$\begin{pmatrix} \mathbf{v}_{\text{r}} \\ \mathbf{v}_{\text{d}} \end{pmatrix} = \begin{pmatrix} \epsilon_{\text{r}}^{-1} \tilde{\mathbf{T}}_{\text{ru}} \epsilon_{\text{u}} & \epsilon_{\text{r}}^{-1} \tilde{\mathbf{T}}_{\text{rp}} \epsilon_{\text{p}} \\ \epsilon_{\text{d}}^{-1} \tilde{\mathbf{T}}_{\text{du}} \epsilon_{\text{u}} & \epsilon_{\text{d}}^{-1} \tilde{\mathbf{T}}_{\text{dp}} \epsilon_{\text{p}} \end{pmatrix} \begin{pmatrix} \mathbf{v}_{\text{u}} \\ \mathbf{v}_{\text{p}} \end{pmatrix} = \begin{pmatrix} \mathbf{T}_{\text{ru}} & \mathbf{T}_{\text{rp}} \\ \mathbf{T}_{\text{du}} & \mathbf{T}_{\text{dp}} \end{pmatrix} \begin{pmatrix} \mathbf{v}_{\text{u}} \\ \mathbf{v}_{\text{p}} \end{pmatrix}. \quad (2.12)$$

It is evident from Eq. 2.12, that the internal dynamics of \mathbf{T} may deviate from the correct internal dynamics $\tilde{\mathbf{T}}$ in dependence of the considered frequency f . Based on these definitions,

general requirements for applying the method MBI^{hc} can be drawn.

As the correct internal dynamics are not measurable in test-rigs, explicit correction of the internal errors ϵ_i by various corrections $\Sigma_i = (\epsilon_i)^{-1}$ is generally not feasible. However, each error ϵ_i contributes to the deviation of \mathbf{C}^c from the correct global dynamics $\tilde{\mathbf{C}}^c$, denoted as $\epsilon(\mathbf{C}^c)$ according to Eq. 2.10. There is a subset of well observable internal errors ϵ_i for $i \in \{u, d, p, r\}$, which mainly determine the global error estimates described in Eq. 2.4. Likewise, another subset of errors may change the internal dynamics but is hardly observable in the global dynamics of \mathbf{C}^c . Therefore, the better the observability of internal errors ϵ_i , the better the achievable compensation by applying the correction Σ^c as depicted in Fig. 2.2.

Regarding the previous definitions, we can further specify the prerequisites for successfully applying the extended MBI in Fig. 2.2. MBI^{hc} is rewarding if it holds that $\epsilon_i^c = \epsilon_i^h$ for $i \in \{u, d, r, p\}$, i.e. the LOM maintains similar structural errors of the internal dynamics over a wide range of operating conditions. As a result, the identical correction can be applied to the hot LOM, i.e. $\Sigma^h = \Sigma^c$. The correction compensates the globally observable internal errors ϵ_i^h of the hot LOM. Accordingly, the improvement of the MBI^{hc} against MBI^h correlates with (1) the observability of internal errors and (2) the sensitivity of the systematic errors ϵ_i of the LOM to changes in operating conditions.

3 Modeling of the thermoacoustic test rig

Table 3.1: Operating condition of SCARLET. 'H' indicates the specific set of hot operating conditions, 'C1' and 'C2' comprise consistent and inconsistent cold operating conditions, respectively.

Parameter	Value			Unit
	H	C1	C2	
Inlet pressure	25	25	18.8	bar
Inlet mass flow	3	3	2.8	kg s ⁻¹
Inlet temperature	825	825	775	K
Thermal power	4.2	-	-	MW

In this section, we describe the complex SCARLET test-rig and recap the modeling of its acoustics with a low-order model necessary for the inference of the FTM. We further identify systematic errors in the modeling of the combustion chamber, that are based on major simplifications or uncertain input parameters.

3.1 Setup of the SCARLET test-rig

The FTM identification techniques in this work are strongly oriented towards application in complex test rigs, as shown in Fig. 3.1. A more detailed description of the installed equipment and functionalities can be found in [1, 10, 11]. Measurements in this test rig can be made under realistic operating conditions as listed in the table 3.1. The table covers inlet conditions before the combustion chamber, including reactive (H) and non-reactive (C1, C2) measurements used in this work (Sec. 4, Sec. 5). Inlet pressures up to 30 bar and preheating temperatures up to 950 K can be achieved with an air mass flow of 4 kg/s. Two microphone arrays are installed to pick up acoustic pressure fluctuations before and after the combustion chamber. The pressure signals can be post-processed using the classical MMM [30] from which the hot and cold combustor transfer matrices, $\tilde{\mathbf{C}}^h$ and $\tilde{\mathbf{C}}^c$, are obtained in a range $f \in [0\text{Hz}, 1000\text{Hz}]$. For reasons of confidentiality, all frequencies f are non-dimensionalized with the injector length L_{ref} and the upstream velocity of air flow, u_{ref} ,

$$\text{St} = f \frac{L_{\text{ref}}}{u_{\text{ref}}}, \quad (3.1)$$

Fig. 3.2 shows the measurement of the hot and cold combustor matrices, $\tilde{\mathbf{C}}^h$, \mathbf{C}^{C1} (C1) and

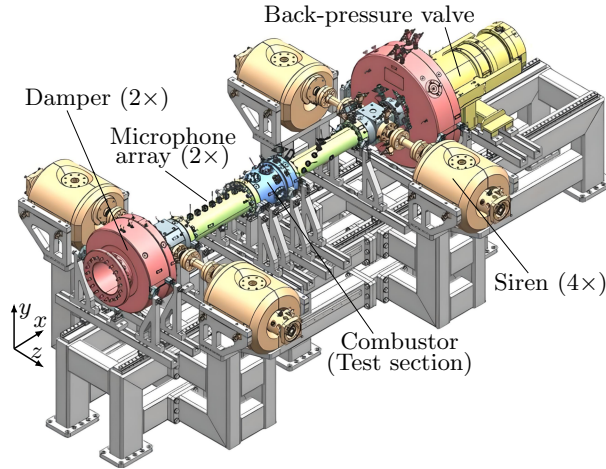


Figure 3.1: Isometric view of SCARLET-test rig considered in this study (flow in x-direction). Figure adapted from Eder *et al.*[11]

C_2^C (C_2). The differences in the inlet conditions manifest as a small shift in the phase and gain of the FTM coefficients. The deviations are more pronounced with increasing St , while the overall trend in the coefficients remains qualitatively the same. The coefficients of the hot measurement differ greatly from those of the cold measurements. Significantly higher gains are obtained for high frequencies in particular.

In addition, a variety of measurement devices are distributed throughout the system. As a result, relevant mean flow quantities such as pressure drops, temperature and mass flows are available. This opens up the possibility of creating sophisticated physically based models, as suggested by Eder *et al.*[10, 11]. Furthermore, the combustor chamber shown in blue in Fig. 3.1 differs strongly from simple test rigs, as it contains both comprehensive cooling mechanisms and a much more complex geometry than standardized test rigs [13, 14]. In the next section, we will briefly recapitulate the advanced features of the combustor chamber. We then explain the physical modeling approaches for incorporating these features into a low-order network model required for an MBI-method, such as MBI^h or MBI^{hc} .

3.2 Low-order network modeling of the SCARLET test rig

A schematic view of the complex geometry and flow phenomena inside the combustor chamber (blue) is illustrated in Fig. 2.1, encompassing bypass-flow and effusion hole cooling. The LOM in this work is built within the publically accessible framework 'taX'[12] and is comprised of multiple acoustic scattering elements (ducts, area jumps...). The main constituents of the LOM representing the test rig are 1D-duct elements, interconnected to reflect the mean-flow paths in the real test-rig. Lumped mean flow quantities of the components are computed based on measurement data gained in and outside the combustor chamber (Δp , T , $m...$) and geometric extensions of the corresponding components of the test rig (lengths, areas...). Unless for the injector, the LOM accounts for the precise combustor geometry. The mean flow is

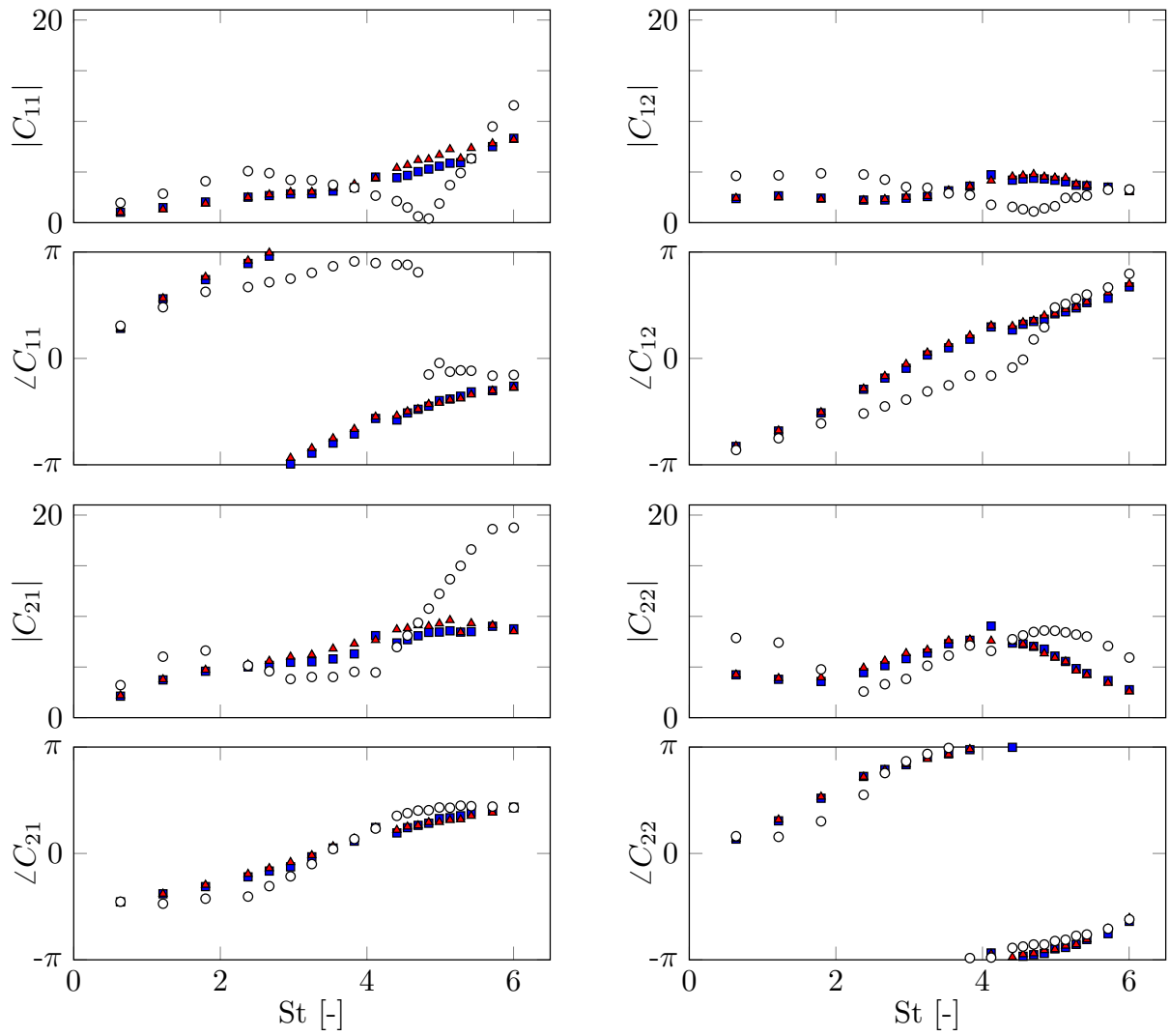


Figure 3.2: Measurements of the hot combustor transfer matrix $\tilde{\mathbf{C}}^h$ (\circ) and cold combustor matrices $\tilde{\mathbf{C}}^c$ for consistent inlet condition C1 (\blacksquare), and inconsistent inlet conditions C2 (\blacktriangle).

governed by the flow splits and the effusion hole cooling mechanism, from which the acoustic behavior of the network elements is derived. The modeling approach is explained in more detail in [10] and specifically by Eder *et al.*[11].

Fig. 3.3 shows phase and gain of the coefficients of \mathbf{C}^c (C1) and \mathbf{C}^c (C2) gained by the LOM in this work (Eq. 2.5). They are compared to the measurements $\tilde{\mathbf{C}}^c$ (C1,C2) in Fig. 3.2. The results suggest, that the global dynamics, particularly in the low-frequency regime, are well described by the model. The phase is met very accurately over the entire frequency spectrum. Even for higher frequencies, i.e. $St > 4$, major characteristics of global dynamics are captured. However, evaluation of the error $\epsilon(\mathbf{C}^c)$ shows, that the overall accuracy successively decreases for higher frequencies regardless of the specific operating conditions of the model.

3.3 Identification of substantial systematic modeling errors

In this work, we revisit the acoustic modeling of the combustion chamber with regard to the study conducted in the following Sec. 4. We identify structures within the LOM, that represent a major reduction of complexity compared to the real test rig (Fig. 3.1, Fig. 2.1) or employ input parameters with high uncertainty of the LOM. On one hand, the utilized LOM comprises network elements, such as the one-dimensional duct elements upstream and downstream, that model the acoustics of the real test rig with high fidelity (Fig. 3.1, green colored) [12, 26]. These elements slightly impair the inference procedure. On the other hand, network elements corresponding to the complex combustion chamber (Fig. 2.1) require substantial simplification or employ input parameters with high uncertainty. These elements have a stronger impact on a systematic deterioration of the inference procedure.

The five circular distributed axis-swirl injectors are represented by a 1D duct-element of length l_{comb} embedded by compact acoustic impedances based on the $l-\zeta$ model [15, 30], with negligible entry length. Thereby, the measurable effective area of the combustor, A_{eff} , determines the cross-section in this simplistic model, while acoustic loss coefficients ζ are determined from the pressure drop over the injector[11]. Considering the extensive simplification, the modeling of the injector is expected to induce a significant systematic modeling error in the network model. Due to the high amount of abstraction between a cross-section of a duct element and an effective area of a complex injector geometry, perturbations of A_{eff} represent a subset of the systematic modeling errors evaluated in Sec. 4.

Furthermore, the flow through the numerous, tiny effusion holes indicated in Fig. 2.1 is represented by n acoustic pathways. The pathways are comprised by consecutive area-jumps and duct elements [10] with cross-sections depending on the perforation in the linear ($l-\zeta$ -model based on measured pressure drop over the liner)[11]. A higher number of acoustic pathways, n , leads to a more gradual approximation of the convergent part of the combustion chamber. n_1 and n_2 independently determine the acoustic pathways in the non-divergent and divergent part of the chamber, respectively, and sum up to n , i.e., $n = n_1 + n_2$. In this model, a serial connection of duct-elements with diminishing cross-section and equal length extends the geometry in the flow direction. The model exhibits significant variation in the geometric representation of the combustor chamber, in particular for variations of n_2 . Likewise, the lo-

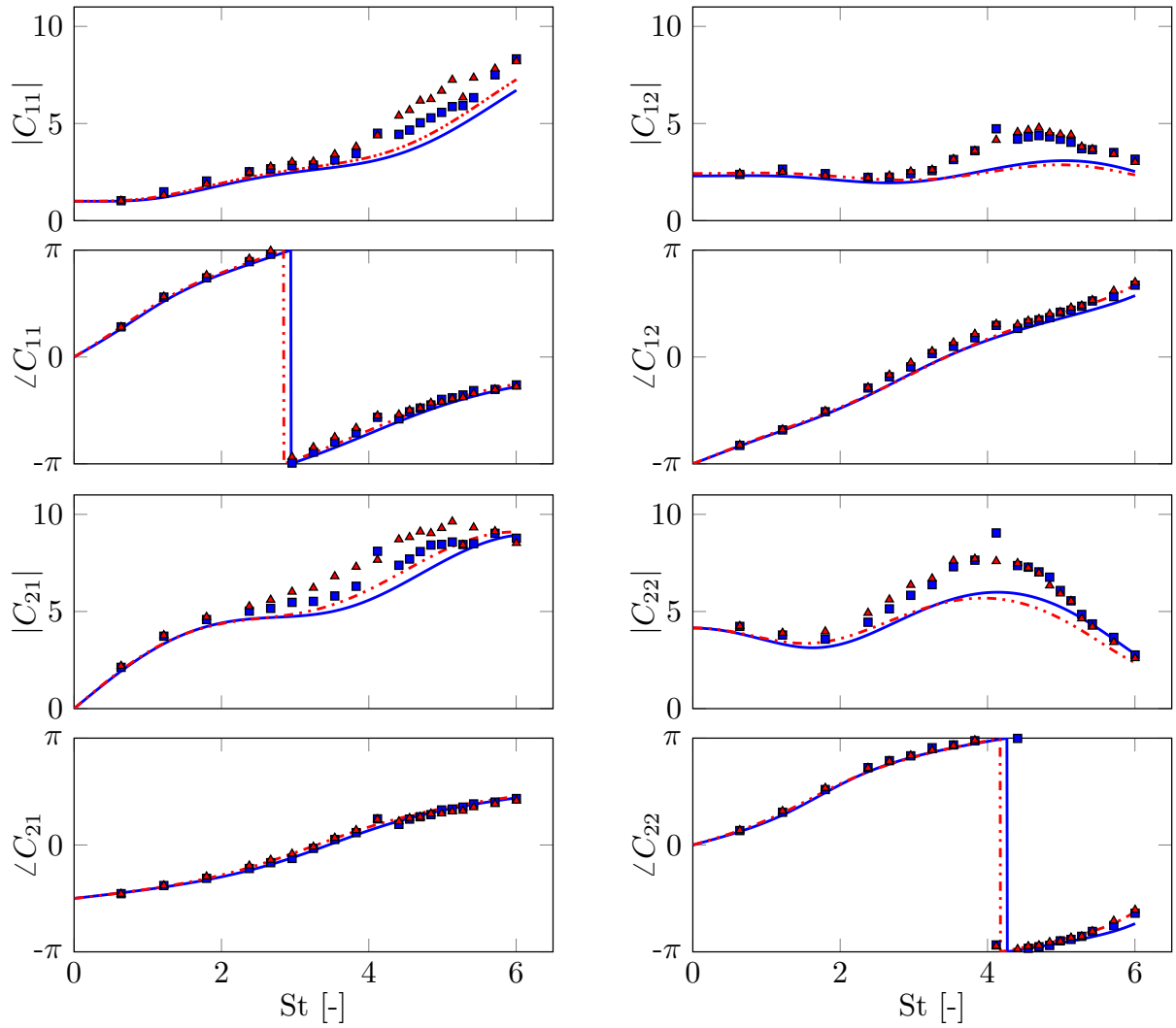


Figure 3.3: Measurements of cold combustor matrices $\tilde{\mathbf{C}}^c$ for consistent inlet condition C1(■), and inconsistent inlet conditions C2(▲) compared to combustor transfer matrices \mathbf{C}^c of inlet conditions C1 (—) and C2 (---) as functions of the Strouhal number St

cal acoustic impedance within the perforated liner is sensitive to n_1 and n_2 .

Finally, the flow-split upstream of the combustion chamber, denoted as X , cannot be determined precisely by experiment. Likewise, variations in the corresponding parameter in the LOM, also denoted as X , extensively impact mean flow quantities inside and outside the combustion chamber. The acoustic scattering matrices of a majority of the network elements systematically change depending on the parameter X . As a result, changes in the parameters $Z = \{X, A_{\text{eff}}, n_1, n_2\}$, represent meaningful systematic modeling errors to be employed in the following study of Sec. 4.

4 Generic investigation with self-consistent LOM framework

This section covers a statistical investigation of the novel method MBI^{hc} , exclusively based on synthetic data, including a synthetic FTM constructed from a predefined FTF (Sec. 4.1). The novel method MBI^{hc} and the model-based inference MBI^{h} [11] are employed for systematically disturbed hot and cold LOMs. The identified FTMs can then be compared to the reference solution to quantify the accuracy of each procedure (Sec 4.2). The numerical experiments are conducted for consistent and inconsistent inlet conditions of the cold LOM. Further, the sensitivity of the inferred FTM to errors in the hot combustor transfer matrix is evaluated for the methods MBI^{h} and the novel method MBI^{hc} (Sec. 4.3). Finally, the statistical study validates the underlying assumption of correlated systematic modeling errors in the LOM (Sec. 4.4).

4.1 General procedure of the statistical study

To create a self-consistent data set for this numerical experiment, a correct FTM, $\tilde{\mathbf{F}}$ is defined based on the Rankine-Hugonot relations [16, 26] of Eq. 4.1. The temperature jump across the compact flame is given by $\theta = (T_{\text{h}}/T_{\text{c}} - 1)$, with T being the temperature, ρc the acoustic impedance, and M the Mach number,

$$\mathbf{F}_{\text{RH}} = \begin{pmatrix} \frac{\rho_{\text{c}}c_{\text{c}}}{\rho_{\text{h}}c_{\text{h}}} & -\theta M_{\text{h}}(1 + \mathcal{F}(\omega)) \\ -\gamma\theta M_{\text{c}} & 1 + \theta\mathcal{F}(\omega) \end{pmatrix}. \quad (4.1)$$

The closure-equation for the heat-release rate is provided by a velocity-sensitive flame transfer function (Eq. 4.2),

$$\mathcal{F}(\omega) \equiv \frac{\dot{Q}'(\omega)/\bar{Q}}{u'_{\text{c}}(\omega)/\bar{u}_{\text{c}}}. \quad (4.2)$$

The flame transfer function \mathcal{F}^* is predefined based on the distributed time delay (DTD) model [11, 28] of a partially premixed flame and depicted in Fig. 4.1. The overall methodology of this investigation is demonstrated in Fig. 4.2. First, an arbitrary LOM of the SCARLET-rig (Sec. 3) is constructed, serving as a benchmark for this investigation. The correct internal dynamics of the cold model are characterized by $\tilde{\mathbf{T}}^{\text{c}}$. The reference dynamics of the hot LOM are given by $\tilde{\mathbf{T}}^{\text{h}}$. The consistent global combustor transfer matrices, $\tilde{\mathbf{C}}^{\text{c}}$ and $\tilde{\mathbf{C}}^{\text{h}}$ can be constructed based on the predefined $\tilde{\mathbf{F}}$. Structural errors are induced in the cold and hot LOMs by integrating randomized, identical parameter variations. These variations are selected in

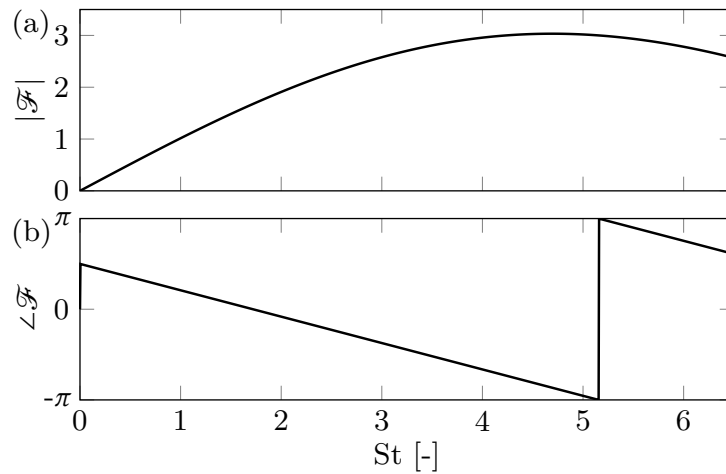


Figure 4.1: (a) Gain and (b) phase of the generic flame transfer function \mathcal{F}^* . Figure adapted from Eder *et al.*[11]

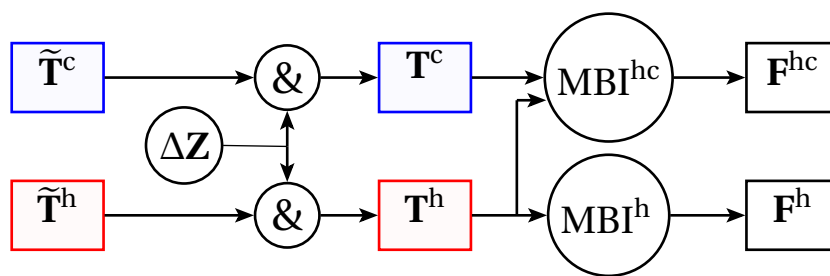


Figure 4.2: Perturbations of hot and cold LOMs ($\tilde{\mathbf{T}}^c, \tilde{\mathbf{T}}^h$) with systematic errors ΔZ leading to disturbed models ($\mathbf{T}^c, \mathbf{T}^h$) utilized for inverse identification. \mathbf{F}^h and \mathbf{F}^{hc} are obtained by applying the methods MBI^h and MBI^{hc} , respectively.

accordance with Sec. 3.3 to provoke substantial deviations in the entire internal dynamics of the disturbed models, denoted as \mathbf{T}^c and \mathbf{T}^h . The parameter variation includes parameters that are either not directly measurable, or induced as part of a simplistic modeling approach (Sec. 3.3). Referring to the reference values of these parameters as \tilde{Z} , a randomized structural error ΔZ is imposed to obtain the parameters of a disturbed hot and cold LOM, denoted as $Z = \tilde{Z} + \Delta Z$. Consequently, the disturbed parameter vector Z follows a uniform distribution centered around \tilde{Z} . In alignment with the LOM proposed by Eder et al. [11], ΔZ includes variations in (1) the mass flow ratio between air entering the combustion chamber and air passing through the annulus (2) the effective area of the injector within a $l - \zeta$ -model [15, 30] (3) the number of acoustic paths representing the numerous effusion holes within the perforated liner. For each sample of disturbed LOMs, \mathbf{T}^c and \mathbf{T}^h , the FTM is identified employing both MBI^h and MBI^{hc} . Eventually, the reconstructed flame transfer matrices, \mathbf{F}^h and \mathbf{F}^{hc} , can be compared to the correct solution $\tilde{\mathbf{F}}$.

4.2 Comparison of MBI-methods by inspection of the identified FTM-elements

The procedure from the previous section is applied to a self-consistent dataset comprising 50 randomized samples of consistent systematic disturbances ΔZ of the hot and cold LOM. In accordance with Fig. 4.2, flame transfer matrices are identified and referred to as \mathbf{F}^h for the method MBI^h , and as \mathbf{F}_{C1}^{hc} and \mathbf{F}_{C2}^{hc} for an identification with method MBI^{hc} using either the consistent inlet conditions 'C1' or inconsistent inlet conditions 'C2' specified in table 3.1. Note, that mean value of the disturbances, $E[\Delta Z]$, approaches zero for $N \rightarrow \infty$. Likewise, both methods identify the correct FTM statistically, i.e. $E[\mathbf{F}]_{N \rightarrow \infty} = \tilde{\mathbf{F}}$. Consequently, higher order moments, for instance, the sample variance $E_N[\epsilon(\mathbf{F})^2]$ based on Eq. 2.10, serve as indicators of the quality of the underlying method [20].

Figure 4.3 compares the gain and phase of the four FTM coefficients of FTMs identified with disturbed cold and hot LOMs. Confidence intervals for \mathbf{F}^h (---), \mathbf{F}^{hc} (---) with consistent inlet conditions 'C1' and \mathbf{F}^{hc} (---) with inconsistent inlet conditions 'C2' are drawn with respect to $\tilde{\mathbf{F}}(-)$. The established decrease of the 95% confidence-interval around $\tilde{\mathbf{F}}$ for the method MBI^{hc} highlights the significant increase in accuracy compared to the accuracy of MBI^{hc} . The confidence intervals scale with $E_N[\epsilon(\mathbf{F})^2]$ and are noticeably smaller for the method MBI^{hc} , even if the inlet conditions are inconsistent for the cold LOM. For instance, considering the F_{22} -element, the confidence interval of MBI^h (---) encompasses the confidence intervals of the extended method MBI^{hc} , regardless of the specific inlet conditions of the cold model. The same conclusion is valid for the majority of frequencies in the coefficients F_{12} and F_{11} . Note, that identification errors $\|(\mathbf{F} - \tilde{\mathbf{F}})\|_\infty$ by far exceed the magnitude of coefficient F_{11} , precluding clear conclusions to be drawn from this coefficient. Particularly at high frequencies, the correction with Σ^c stabilizes the identification procedure, allowing for efficient correction of physically implausible high gains, as observed in the method MBI^h for coefficient F_{12} . Furthermore, the accuracy of \mathbf{F}_{C1}^{hc} statistically matches the accuracy of \mathbf{F}_{C2}^{hc} . The selection of

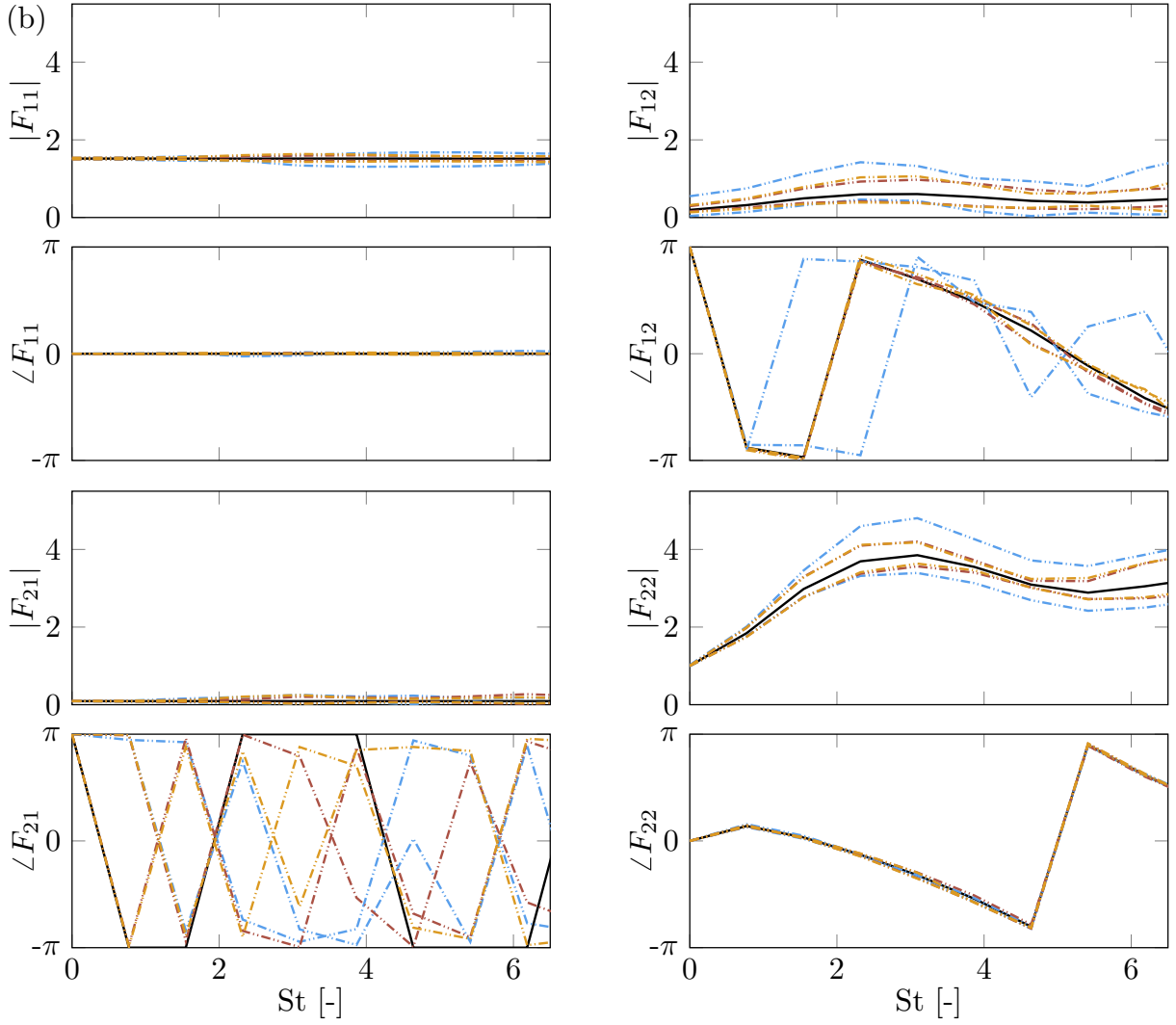


Figure 4.3: Confidence intervals (95%) around the reference solution $\tilde{\mathbf{F}}(-)$ for gain and phase of the coefficients of the identified FTM obtained with different extraction methods MBI^h (---), MBI^{hc} with consistent inlet conditions(---), MBI^{hc} with deviating inlet conditions(---) according to table 3.1. Data is based on 50 samples of disturbed hot and cold LOMs within the generic SCARLET-framework.

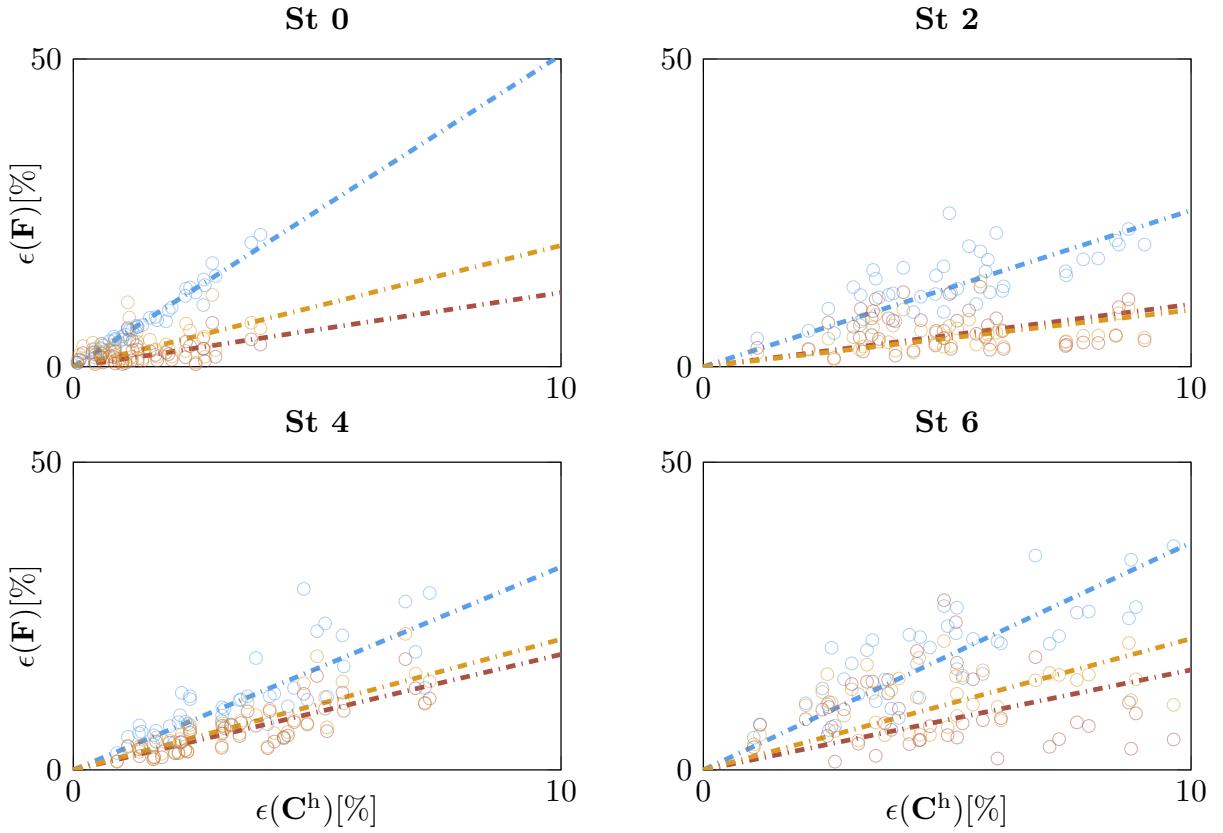


Figure 4.4: Relative error (Eq. 2.10) of the identified FTM for different extraction methods within the generic framework based on the SCARLET-model: MBI^h (---), MBI^{hc} with consistent inlet conditions(---), MBI^{hc} with deviating inlet conditions(---) according to table 3.1.

inconsistent inlet conditions 'C2' instead of consistent inlet conditions 'C1' does not significantly impair prediction. This suggests that the presumed linear correlation between Σ^c and Σ^h is robust against deviations in inlet conditions, even considering deviations of 7-25% in the upstream flow conditions of the combustion chamber (table 3.1). Such an inherent system property of the utilized LOMs is advantageous for an application to real measurement data. As shown in this study, a statistical investigation can validate or disprove it prior to the inference of \mathbf{F} .

4.3 Sensitivity analysis of model-based inference methods

The error $\epsilon(\mathbf{F})$ is correlated with the error $\epsilon(\mathbf{C}^h)$, which is typically undisclosed, except within the confines of this synthetic framework. Thus, this study explicitly evaluates the relationship between these errors, as depicted in Fig. 4.4. The figure shows $\epsilon(\mathbf{F})$ for \mathbf{F}^h (---), \mathbf{F}^{hc} (---) with consistent inlet conditions 'C1' and \mathbf{F}^{hc} (---) with inconsistent inlet conditions. The corre-

sponding error $\epsilon(\mathbf{C}^h)$ is drawn along the horizontal direction for four different Strouhal numbers St . Since the methods consistently identify the FTM for $\epsilon(\mathbf{C}^h) = 0$, a linear regression through the origin is employed. Higher slopes of the linear fits at a certain frequency indicate less accurate determination of \mathbf{F} statistically. Notably, applying either MBI^{hc} with consistent inlet conditions (---) or MBI^{hc} with inconsistent inlet conditions (---) leads, on average, to significantly more accurate results than applying MBI^{h} (---). The methods become more distinguishable, particularly for high errors $\epsilon(\mathbf{C}^h)$. The relative spread of the samples decreases, making it even less likely to observe $\epsilon(\mathbf{F}^{\text{h}}) < \epsilon(\mathbf{F}^{\text{hc}})$ for a specific sample of the dataset.

A comparison of the distinct frequencies (Eq. 3.1) shows, that the applied structural disturbances ΔZ cause systematic errors which are strongly dependent on St . While the samples in Fig. 4.4 are clustered between $\epsilon(\mathbf{C}^h) = [0\%, 4\%]$ for $St = 0$, errors $\epsilon(\mathbf{C}^h)$ up to 10% are observed for higher frequencies. This observation explains, why the visual inspection of gain and phase in the low-frequency limit (Fig. 4.3) implies highly accurate identification of \mathbf{F} regardless of the utilized procedure. Note, that the established correlation between $\epsilon(\mathbf{F})$ and $\epsilon(\mathbf{C}^h)$ further highlights the requirement of an accurate model utilized in any model-based inference approach. We conclude from the given data, that minimizing $\epsilon(\mathbf{C}^h)$ is most efficient regardless of the inference method, while the identification is statistically more accurate for a given value of $\epsilon(\mathbf{C}^h)$ if the novel MBI^{hc} -approach is followed. The value of $\epsilon(\mathbf{C}^h)$ is not accessible outside this generic framework. Therefore, we investigate the statistical correlation between $\epsilon(\mathbf{C}^h)$ and the error $\epsilon(\mathbf{C}^c)$, which can be assessed even in an experimental framework[11].

4.4 Correlation of systematical errors for hot and cold operating conditions

Accordingly, Fig. 4.5 shows the statistical relation between the errors $\epsilon(\mathbf{C}^h)$ and $\epsilon(\mathbf{C}^c)$. The N samples of errors $\epsilon(\mathbf{C}^c)$ are drawn over the error $\epsilon(\mathbf{C}^h)$ for corresponding ΔZ_i . The data is complemented with a linear regression (MBI^{hc} with 'C1' (---), MBI^{hc} with 'C2' (---)). A linear relation for identical errors $\epsilon^{\text{h}} = \epsilon^{\text{c}}$ is added as a reference (-).

A similar correlation is established for the consistent and inconsistent operating conditions, 'C1' and 'C2'. This correlates with the similar error reduction of these methods in Fig. 4.3. On average, $\epsilon(\mathbf{C}^c)$ tends to be smaller than $\epsilon(\mathbf{C}^h)$, while the correlation coefficient shows strong dependency on St . In particular for high frequencies, the slope of the linear regression increases accompanied by greater dispersion of the samples. Fig. 4.5 confirms the assumption of linear correlation between the errors ϵ^{c} and ϵ^{h} , making the applied correction, $\Sigma^{\text{h}} \approx \Sigma^{\text{c}}$ (Fig. 2.2), plausible. The data indicates, that the prominent improvements of MBI^{hc} against MBI^{h} become evident in the relation between $\epsilon(\mathbf{C}^h)$ and $\epsilon(\mathbf{C}^c)$ in Fig. 4.5. Consider $St = 2$ compared to $St = 4$, where the spread of samples around the linear regression for $St = 4$ is less than the sample deviation for $St = 2$. Moreover, Fig. 4.5 verifies that the error ϵ^{c} is a meaningful indicator for the error $\epsilon(\mathbf{F})$, due to the evident correlation between $\epsilon(\mathbf{C}^h)$ and $\epsilon(\mathbf{C}^c)$. Equivalently, optimizing a LOM at non-reactive conditions through parameters fitting [1] or by improving a physical model [11] is well justified in the scope of model-based inference approaches.

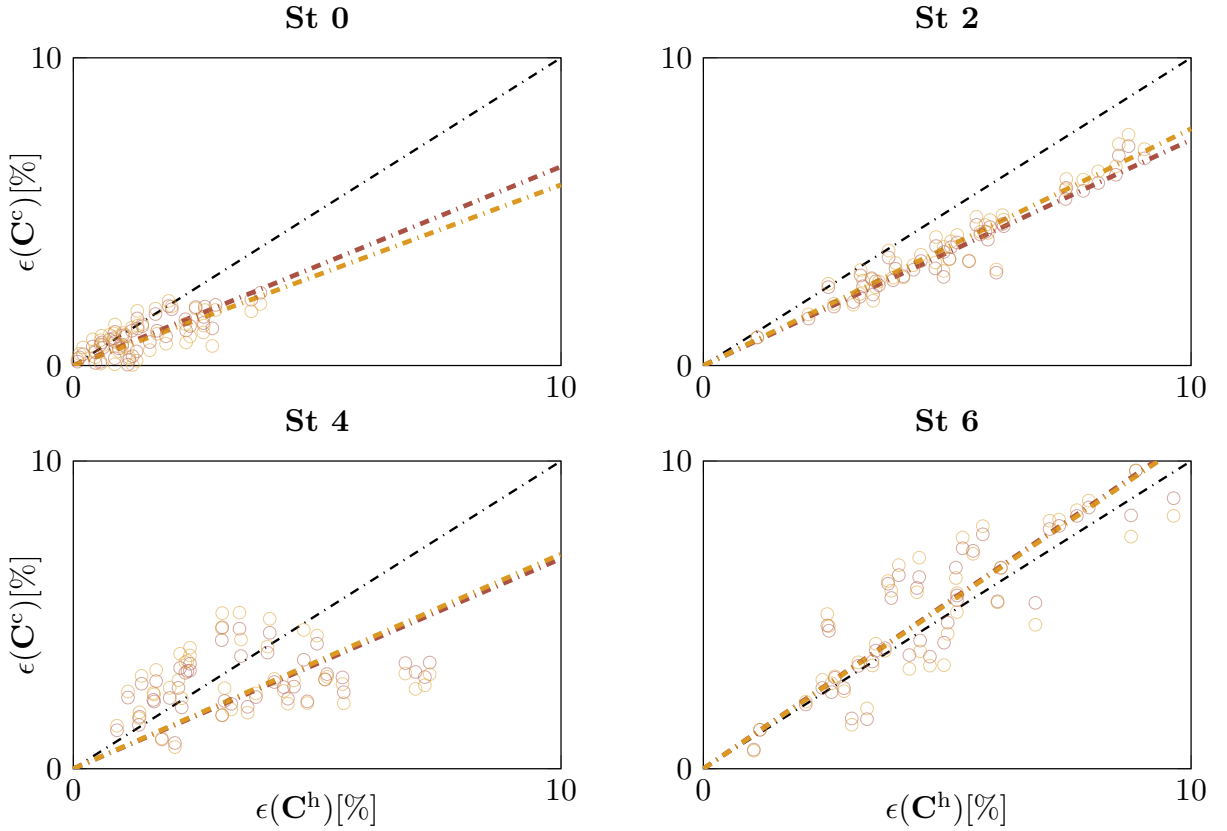


Figure 4.5: Relative error $\epsilon(\mathbf{C}^c)$ (Eq. 2.10) cold combustor transfer matrix over the relative error of the hot combustor transfer matrix $\epsilon_{\text{rel}}(\mathbf{C}^h, \tilde{\mathbf{C}}^h)$ for different inlet conditions of the cold LOM: MBI^{hc} with consistent inlet conditions 'C1' (---), MBI^{hc} with deviating inlet conditions 'C2' (---) according to table 3.1. Data is based on 50 samples of randomly disturbed hot and cold LOMs within the generic SCARLET-framework.

5 FTM inference with experimental data

In the following study, we apply the novel method MBI^{hc} to measurement data of the SCARLET test-rig [13, 14]. Data includes a single hot measurement $\tilde{\mathbf{C}}^{\text{h}}$ and two measurements $\tilde{\mathbf{C}}^{\text{c}}$ at different operating conditions (table 3.1) for application of the extended method MBI^{hc} . This aims to investigate, whether coincident inlet conditions are an inevitable prerequisite for applying the procedure MBI^{hc} in practical applications. Considering the experimental data, measurement errors impede the correct identification of the FTM. Note, that statistical errors of hot and cold measurements contribute to \mathbf{F}^{hc} , while systematic errors can be potentially eliminated when utilizing MBI^{hc} . On the contrary, MBI^{h} is solely affected by statistical measurement errors related to the measurement of $\tilde{\mathbf{C}}^{\text{h}}$.

5.1 Identification of FTM applying different procedures

The LOM elucidated in Sec. 3 was first employed by Eder et al [11] to identify a FTM from real measurement data of the SCARLET test-rig. To maintain comparability with recent results, the identical hot and cold measurements, $\tilde{\mathbf{C}}^{\text{h}}$ and $\tilde{\mathbf{C}}^{\text{c}}$, and the same operating conditions, i.e. 'H1' and 'C1' (table 3.1) are considered in this work. A second cold measurement 'C2' according to table 3.1 is used in the extended inference method MBI^{hc} . Refer to Fig. 3.2 for the measured $\tilde{\mathbf{C}}^{\text{h}}$ and $\tilde{\mathbf{C}}^{\text{c}}$ and Fig. 3.3 for the modeled \mathbf{C}^{c} at the considered operating conditions. The study in Sec. 4 revealed, that the error $\epsilon(\mathbf{C}^{\text{c}})$ correlates with the error $\epsilon(\mathbf{C}^{\text{h}})$ (Fig. 4.5) and, consecutively, with the error $\epsilon(\mathbf{C}^{\text{h}})$ (Fig. 4.4). An explicit correlation as in Fig. 4.4 is not applicable, prohibiting quantitative assessments of $\epsilon(\mathbf{F})$ unless the generic results of the synthetic study are taken as a reference.

Fig. 5.1 gives an overview of the different identification procedures applied to the experimental data. As a reference, the FTM obtained with the BFTM-approach [4], is plotted (\times). Previous work has shown that this approach is generally not applicable to complex test rigs such as the SCARLET test-rig in this work [10]. Further, the FTM \mathbf{F}^{h} identified with the method MBI^{h} is visualized using blue triangles (\blacktriangle). In agreement with the results of Eder *et al.* [11], the method computes \mathbf{F}^{h} substantially deviating in gain from the FTM obtained with the BFTM-approach. The FTMs identified with the novel method MBI^{hc} are drawn in red circles (\bullet) for the consistent inlet conditions 'C1'. White circles (\circ) indicate results based on the inconsistent inlet conditions 'C2'. Comparing $\mathbf{F}_{\text{C1}}^{\text{hc}}$ and $\mathbf{F}_{\text{C2}}^{\text{hc}}$, we observe that the coefficients very closely match in the low-frequency regime of $\text{St} < 2$, still showing good agreement up to $\text{St} = 4.5$. This implies, that similar corrections Σ^{c} (Eq. 2.8) are applied in this regime, i.e. $\Sigma_{\text{C1}}^{\text{c}} \approx \Sigma_{\text{C2}}^{\text{c}}$. The LOMs share small systematic errors of similar amplitude and phase in the limit $f \rightarrow 0$ for operating conditions 'C1' and 'C2'. This observation further matches the results in Fig. 4.5, indicating that

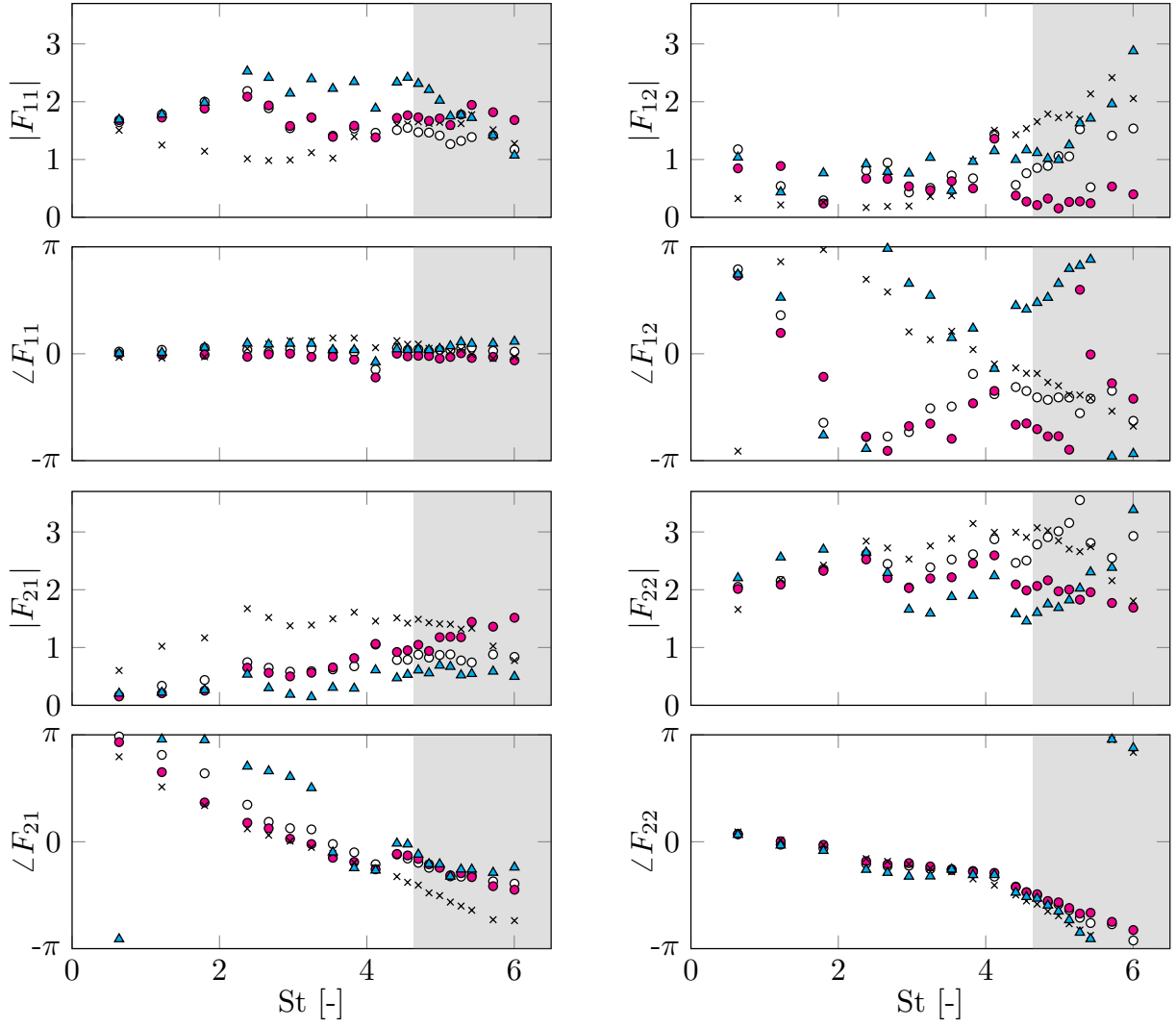


Figure 5.1: Comparison of gain and phase of the identified FTMs for a given hot measurement $\tilde{\mathbf{C}}^h$ applying the BFTM-approach (x) using $\tilde{\mathbf{C}}^c$ with operating conditions 'C1' as cold combustor transfer matrix, the MBI^h -method (Δ), MBI^{hc} based on $\tilde{\mathbf{C}}^c(\text{C1})$ (\bullet), and MBI^{hc} based on $\tilde{\mathbf{C}}^c(\text{C2})$ (\circ). Following Eder *et al.* [11], the model-based inference is considered as inaccurate for $\text{St} > 4.5$ (gray)

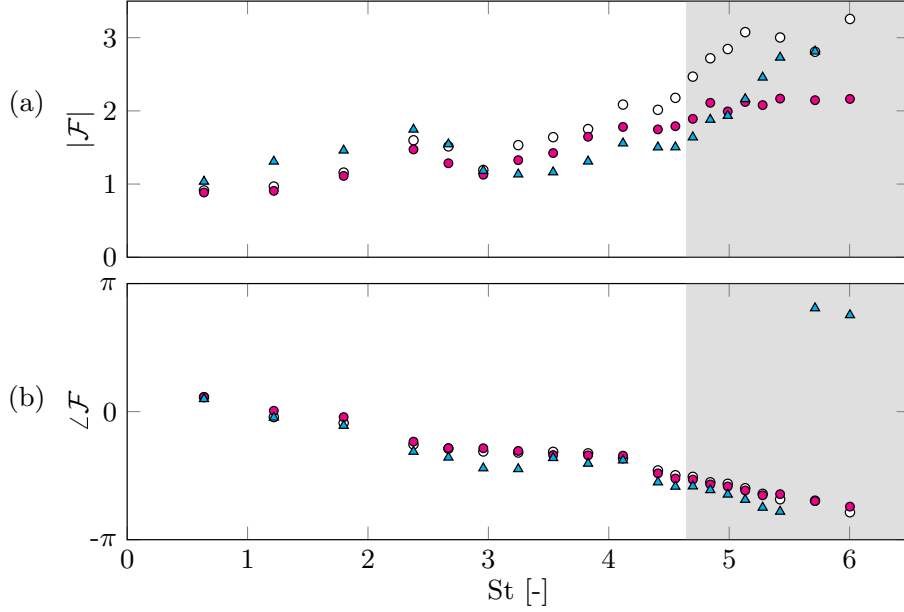


Figure 5.2: Comparison of gain and phase of the identified FTFs for a given hot measurement $\tilde{\mathbf{C}}^h$ using $\tilde{\mathbf{C}}^c$ (C1) as cold combustor transfer matrix, the MBI^h -method (\blacktriangle), MBI^{hc} based on $\tilde{\mathbf{C}}_{\text{C1}}^c$ (\bullet), and MBI^{hc} based on $\tilde{\mathbf{C}}_{\text{C2}}^c$ (\circ).

$\epsilon(\mathbf{C}^c)$ is insensitive to the specific choice of inlet conditions. In the high-frequency regime, the respective FTFs diverge. The gain in the coefficients F_{11} and F_{21} are higher for the consistent conditions 'C1', whereas the gain in the coefficients F_{12} and F_{22} are significantly higher for inconsistent conditions 'C2'.

The main focus in this study is on differences between the method MBI^h and its extension, MBI^{hc} . Fig. 5.1 reveals, that FTFs reconstructed with MBI^{hc} (\bullet, \circ) deviate substantially from the FTF based on MBI^h (\blacktriangle) in all coefficients. The corrections of method MBI^{hc} counteract the strong increase in gain that can be observed for method MBI^h in the coefficients F_{12} and F_{22} . This effect is particularly pronounced for the MBI^{hc} -method based on the consistent cold model (\bullet). In the range $\text{St} < 4.5$, comparable dynamics can only be seen in the F_{12} -element, while the phases of the F_{12} and F_{21} elements in particular do not agree. The choice of method also has a strong effect on the F_{22} element, which is subsequently used to extract the FTF (Eq. 4.1) [2]. With a similar phase up to $\text{St} = 4.5$, the qualitative curve of the amplitude remains very comparable. Nevertheless, the curve when using MBI^{hc} is flattened for both inlet conditions, so frequency-dependent amplitude changes are considerably more gradual. Obviously, there is an outlier in the measurements of $\tilde{\mathbf{C}}^h$ and $\tilde{\mathbf{C}}^c$ near $\text{St} = 4$ (Fig. 3.2), that is reflected in the inferred FTFs, as well.

Furthermore, the FTF \mathcal{F} is extracted from the F_{22} elements applying the Rankine-Hunginot-relations (Eq. 4.1) and assuming a velocity-sensitive flame (Eq. 4.2). It is illustrated in Fig. 5.2. The FTFs exhibit dynamics, that are sensitive to the applied identification procedure. The method MBI^{hc} identifies a very similar FTF regardless of the operating conditions for $\text{St} < 4.5$,

generally flattening out the dynamics compared to the FTF obtained with MBI^h .

5.2 Discussion

The chosen method significantly impacts the dynamics of the identified FTMs. As there is no reference solution for the FTM, $\tilde{\mathbf{F}}$, available for the analyzed data, it is not yet possible to clearly demonstrate an improvement in a real application when using MBI^{hc} compared to MBI^h . The inference with MBI^{hc} exhibits similar features in the synthetic and experimental frameworks, such as the damping of high gains in the high-frequency range of the F_{12} and F_{22} -elements. This implies, that conclusions can be drawn from the synthetic study in Sec. 4. Nonetheless, the applied disturbances ΔZ only represent a subset of theoretically applicable disturbances, to which any conclusion from self-consistent studies will be restricted. The analysis of the utilized LOM showed the statistically improved robustness and accuracy of MBI^{hc} , indicating a preference for MBI^{hc} over MBI^h in an experimental framework. The established relations between $\epsilon(\mathbf{F})$ and $\epsilon(\mathbf{C}^h)$ further revealed that the improvement in accuracy when employing MBI^{hc} instead of MBI^h is even more prominent for higher systematic errors $\epsilon(\mathbf{C}^h)$. The same conclusion can be drawn for higher values of $\epsilon(\mathbf{C}^c)$ employing the strict correlation of the latter errors (Fig. 4.5). For LOMs, that accurately match the global dynamics $\tilde{\mathbf{C}}^c$ (e.g. $\epsilon(\mathbf{C}^c) \ll 10\%$) and include sophisticated acoustic modeling of the internal dynamics, the choice of MBI^h is very reasonable. Note, that deviations from the proposed linear correlation between the cold and hot internal dynamics, \mathbf{T}^h and \mathbf{T}^c , generally lower the reward of the applied correction $\Sigma^h = \Sigma^c$ (Fig. 2.2). Partial fulfillment of this assumption might be sufficient to reduce major errors in global and internal dynamics according to Fig. 4.4. Likewise, the statistical reduction of minor errors is more sensitive to the validity of the correlation assumption. Therefore, the method MBI^h should be favored in case of very small global errors, as the chances of deterioration by employing the method MBI^{hc} become more relevant. Regarding the simplified internal dynamics of LOM utilized in this work (Sec. 3.3) and the accuracy of global dynamics (Fig. 3.3), the novel method MBI^{hc} with consistent inlet conditions for the correction is considered as most reliable in the experimental framework.

Previous work claims that the lack of explicit uncertainty bounds of the identified FTM is a drawback for the applied MBI-methods [11]. So far, the error $\epsilon(\mathbf{C}^c)$ indicates the accuracy of the LOM and is utilized to estimate the accuracy of the inferred FTM, as well. Application of the novel method MBI^{hc} opens new opportunities for estimating the systematic error of \mathbf{F} . For a given frequency f , we propose to evaluate the deviation of \mathbf{F}^h (MBI^h) from \mathbf{F}^{hc} (MBI^{hc}). This difference denoted as $\epsilon(\mathbf{F}^{\text{hc}}, \mathbf{F}^h)$ accounts both for the error $\epsilon(\mathbf{C}^c)$ and the sensitivity of the model-based inference towards the respective error in the global dynamics. As a result, the measure $\epsilon(\mathbf{F}^{\text{hc}}, \mathbf{F}^h)$ weights the global errors by their significance in the model-based inference approach.

Results with experimental (Sec. 5) and synthetic data (Sec. 4) indicate, that the robustness of model-based inference methods increases even for utilizing inconsistent cold operating conditions for a systematic correction (Fig. 2.2). This raises opportunities for determining a generalized correction Σ^c (Eq. 2.8) based on several measurements, even including statistical

procedures. Probabilistic studies with the utilized LOM (Sec. 4) may further be extended to derive meaningfully, how discrepancies of the global dynamics \mathbf{C}^c manifest in the dynamics of \mathbf{F} . Nonetheless, this work again highlights the importance of building physically meaningful LOMs, as this is the only reliable strategy for better post-processing a FTM and consecutively, a FTE.

6 Conclusion and Outlook

Classical model-based inference methods identify the FTM by measuring the hot combustor transfer matrix using a single hot LOM. Therefore, any error in the internal dynamics of the utilized LOM impairs inference accuracy. The novel inference procedure in this work includes a second, cold measurement. This might increase the accuracy of the identified FTM, as partial correction of systematic errors of the hot LOM is achieved. Statistical investigations in a self-consistent framework have demonstrated, that identification of FTMs with the novel inference method is superior to the classical MBI-method. Improvement was even shown if LOMs at substantially different cold operating conditions were utilized for the correction. The presented investigation can be generally used to assess the applicability of the extended inference method based on the intrinsic properties of the employed LOM. Ultimately, MBI methods were applied to measurements of the Rolls-Royce SCARLET test rig, both with and without the proposed systematic correction. The extended inference method was more robust, suppressing a nonphysical gain increase in the high-frequency regime of the FTM-elements. The specific choice of inlet conditions for the cold LOM had a small effect unless there were substantial errors in the dynamics of the LOMs.

We propose an application of the extended model-based inference, particularly for simplistic LOMs that inadequately match the measured global dynamics. Future work could focus on generalizing this correction procedure, which encounters numerous cold measurements and probabilistic concepts. Likewise, developing more sophisticated LOMs, particularly those describing the acoustic feedback loops within the combustion chamber of complex test rigs, could further enhance the post-processing of the FTM.

Bibliography

- [1] Cetin Alanyalioglu, Hanna Reinhardt, André Fischer, Claus Lahiri, Henrik Nicolai, and Christian Hasse. Comparison of acoustic, optic, and heat release rate based flame transfer functions for a lean-burn injector under engine-like conditions. In *Symposium on Thermoacoustics in Combustion*, Zurich, Switzerland, 2023.
- [2] Reddy Alemela, D. Fanaca, Christoph Hirsch, Thomas Sattelmayer, and Bruno Schuermans. Determination and scaling of thermo acoustic characteristics of premixed flames. *International Journal of Spray and Combustion Dynamics*, 2:169–198, 06 2010.
- [3] Pieter Appeltans and W. Michiels. A pseudo-spectra based characterisation of the robust strong H-infinity norm of time-delay systems with real-valued and structured uncertainties. *ArXiv*, September 2019.
- [4] Stefanie Bade, Michael Wagner, Christoph Hirsch, Thomas Sattelmayer, and Bruno Schuermans. Influence of Fuel-Air Mixing on Flame Dynamics of Premixed Swirl Burners. In *ASME Turbo Expo 2014: Turbine Technical Conference and Exposition*, volume 4A: Combustion, Fuels and Emissions, page V04AT04A023, Düsseldorf, Germany, 2014. American Society of Mechanical Engineers.
- [5] Valter Bellucci, Bruno Schuermans, Dariusz Nowak, Peter Flohr, and Christian O. Paschereit. Thermoacoustic Modeling of a Gas Turbine Combustor Equipped With Acoustic Dampers. *Journal of Turbomachinery*, 127(2):372–379, 2005.
- [6] Adi Ben-Israel and Thomas N. E. Greville. *Generalized inverses: theory and applications*. Springer, New York, NY, USA, 2nd edition, 2003.
- [7] J.-P. DALMONT. ACOUSTIC IMPEDANCE MEASUREMENT, PART I: A REVIEW. *Journal of Sound and Vibration*, 243(3):427–439, 2001.
- [8] Ann P. Dowling. Thermoacoustic Instability. In *6th Int. Congress on Sound and Vibration*, pages 3277–3292, Copenhagen, Denmark, 1999.
- [9] Johannes Eckstein and Thomas Sattelmayer. Low-order modeling of low-frequency combustion instabilities in aeroengines. *Journal of Propulsion and Power*, 22(2):425–432, 2006.

-
- [10] Alexander J. Eder, André Fischer, Claus Lahiri, Moritz Merk, Max Stauffer, Ruud Eggels, Camilo F. Silva, and Wolfgang Polifke. Identification of the dynamics of a turbulent spray flame at high pressure. In *Symposium on Thermoacoustics in Combustion*, Zurich, Switzerland, 2023.
- [11] Alexander J. Eder, Moritz Merk, Thomas Hollweck, André Fischer, Claus Lahiri, Camilo F. Silva, and Wolfgang Polifke. Model-based inference of flame transfer matrices from acoustic measurements in an aero-engine test rig. In *ASME Turbo Expo 2024: Turbomachinery Technical Conference and Exposition*, London, England, United Kingdom, 2024.
- [12] Thomas Emmert. *State Space Modeling of Thermoacoustic Systems with Application to Intrinsic Feedback*. PhD thesis, TU München, München, Germany, 2016.
- [13] André Fischer and Claus Lahiri. Ranking of aircraft fuel-injectors regarding low frequency thermoacoustics based on an energy balance method. In *ASME Turbo Expo 2021: Turbomachinery Technical Conference and Exposition*, volume 3B: Combustion, Fuels, and Emissions, page V03BT04A011, Virtual, Online, 2021. American Society of Mechanical Engineers.
- [14] André Fischer, Claus Lahiri, and Thomas Doerr. Design, build, and commissioning of the new thermo-acoustics combustion test rig Scarlet. Technical Report DLRK2017-450116, Rolls-Royce Deutschland, 2017.
- [15] A. Gentemann, A. Fischer, S. Evesque, and W. Polifke. Acoustic transfer matrix reconstruction and analysis for ducts with sudden change of area. In *9th AIAA/CEAS Aeroacoustics Conference and Exhibit*, page 3142, Hilton Head, SC, USA, 2003. AIAA.
- [16] Jakob J. Keller. Thermoacoustic Oscillations in Combustion Chambers of Gas Turbines. *AIAA Journal*, 33(12):2280–2287, 1995.
- [17] J. Lavrentjev, M. Åbom, and H. Bodén. A measurement method for determining the source data of acoustic two-port sources. *Journal of Sound and Vibration*, 183(3):517–531, 1995.
- [18] Moritz Merk and Alexander J. Eder. Personal correspondence via E-Mail (03/28/2024) .
- [19] Moritz Merk and Alexander J. Eder. Personal correspondence in a meeting (03/07/2024) .
- [20] Nicholas Metropolis and S. Ulam. The monte carlo method. *Journal of the American Statistical Association*, 44(247):335–341, 1949.
- [21] Manohar L. Munjal and Allan G. Doige. Theory of a Two Source-Location Method for Direct Experimental Evaluation of the Four-Pole Parameters of an Aeroacoustic Element. *Journal of Sound and Vibration*, 141(2):323–333, 1990.

BIBLIOGRAPHY

- [22] F. Nicoud and T. Poinsot. Thermoacoustic instabilities: Should the Rayleigh criterion be extended to include entropy changes? *Combustion and Flame*, 142(1):153–159, 2005.
- [23] Alessandro Orchini, Tiemo Pedergrana, Philip E. Buschmann, Jonas P. Moeck, and Nicolas Noiray. Reduced-order modelling of thermoacoustic instabilities in can-annular combustors. *Journal of Sound and Vibration*, 526:116808, 2022.
- [24] Christian O. Paschereit and Wolfgang Polifke. Characterization of Lean Premixed Gas Turbine Burners as Acoustic Multi-Ports. In *APS/DFD Annual Meeting*, San Francisco, CA, 1997. APS.
- [25] Christian O. Paschereit and Wolfgang Polifke. Investigation of the Thermo-Acoustic Characteristics of a Lean Premixed Gas Turbine Burner. In *Int'l Gas Turbine and Aeroengine Congress & Exposition*, ASME 98-GT-582, Stockholm, Sweden, 1998. ASME.
- [26] Christian O. Paschereit, Bruno Schuermans, Wolfgang Polifke, and Oscar Mattson. Measurement of Transfer Matrices and Source Terms of Premixed Flames. *Journal of Engineering for Gas Turbines and Power*, 124(2):239–247, 2002.
- [27] M. C. A. M. Peters, A. Hirschberg, A. J. Reijnen, and A. P. J. Wijnands. Damping and Reflection Coefficient Measurements for an Open Pipe at Low Mach and Low Helmholtz Numbers. *Journal of Fluid Mechanics*, 256:499–534, 1993.
- [28] Wolfgang Polifke. Modeling and analysis of premixed flame dynamics by means of distributed time delays. *Progress in Energy and Combustion Science*, 79:100845, 2020.
- [29] Bruno Schuermans, Felix Guethe, Douglas Pennell, Daniel Guyot, and Christian O. Paschereit. Thermoacoustic Modeling of a Gas Turbine Using Transfer Functions Measured Under Full Engine Pressure. *Journal of Engineering for Gas Turbines and Power*, 132(11):111503, November 2010.
- [30] Bruno Schuermans, Wolfgang Polifke, and Christian O. Paschereit. Modeling Transfer Matrices of Premixed Flames and Comparison With Experimental Results. In *ASME 1999 International Gas Turbine and Aeroengine Congress and Exhibition*, volume 2: Coal, Biomass and Alternative Fuels; Combustion and Fuels; Oil and Gas Applications; Cycle Innovations, page V002T02A024, Indianapolis, IN, USA, June 1999. American Society of Mechanical Engineers.
- [31] Dan Zhao. Chapter 1 - Introduction of self-sustained thermoacoustic instability. In Dan Zhao, editor, *Thermoacoustic Combustion Instability Control*, pages 1–112. Academic Press, 2023.